Aerosol Science and Technology

ISSN: 0278-6826 (Print) 1521-7388 (Online) Journal homepage: https://www.tandfonline.com/loi/uast20

Examining Elemental Surface Enrichment in Ultrafine Aerosol Particles Using Analytical Scanning Transmission Electron Microscopy

Andrew D. Maynard , Yasuo Ito , Ilke Arslan , Anthony T Zimmer , Nigel Browning & Alan Nicholls

To cite this article: Andrew D. Maynard , Yasuo Ito , Ilke Arslan , Anthony T Zimmer , Nigel Browning & Alan Nicholls (2004) Examining Elemental Surface Enrichment in Ultrafine Aerosol Particles Using Analytical Scanning Transmission Electron Microscopy, Aerosol Science and Technology, 38:4, 365-381, DOI: 10.1080/02786820490437479

To link to this article: https://doi.org/10.1080/02786820490437479

Published online: 17 Aug 2010.

Aerosol Science and Technology, 38:365–381, 2004

ISSN: 0278-6826 print / 1521-7388 online
DOI: 10.1080/02786820490437479

Examining Elemental Surface Enrichment in Ultrafine Aerosol Particles Using Analytical Scanning Transmission Electron Microscopy

Andrew D. Maynard,[1] Yasuo Ito,[2] Ilke Arslan,[3] Anthony T Zimmer,[1] Nigel Browning,[3] and Alan Nicholls[4]

[1]*National Institute for Occupational Safety and Health, Cincinnati, Ohio*
[2]*Northern University Illinois, Department of Physics, DeKalib, Illinois*
[3]*University of Illinois at Chicago, Department of Physics, Chicago, Illinois*
[4]*University of Illinois at Chicago, Research Resources Center, Chicago, Illinois*

The surface structure and chemistry of ultrafine aerosol particles (typically particles smaller than 100 nm in diameter) play key roles in determining physical and chemical behavior, and is relevant to fields as diverse as nanotechnology and aerosol toxicity. Analytical scanning transmission electron microscopy (STEM) is one of the few analytical methods available that is potentially capable of characterizing ultrafine particles at subnanometer resolution. We propose a method that enables STEM to characterize and quantify elemental surface enrichment within radially symmetrical particles at a spatial resolution of less than 1 nm when used in conjunction with electron energy loss spectroscopy (EELS) and X-ray energy dispersive spectroscopy (EDS). Although the method relies on a number of assumptions for complete particle characterization, estimation of the depth of an outer layer of elemental enrichment should be possible with relatively few assumptions. A preliminary investigation of the method has been carried out using particles from gas metal arc welding on mild steel. Using the analysis method, we were able to characterize Si and O enrichment in a number of particles. Two particles were investigated extensively using EELS and EDS analysis. Both techniques allowed surface enrichment of Si to be identified and quantified in the particles, although the relatively poor sensitivity of EDS was a limiting factor in the analysis. EELS allowed rapid data collection and enabled surface enrichment of Si and O to be characterized. Using a simple model to describe elemental composition with radial position, it was estimated that Si and O were enriched in an outer layer around the particle approximately 1 nm deep.

Received 21 March 2003; accepted 21 January 2004.
Address correspondence to Andrew D. Maynard, National Institute for Occupational Safety and Health, 4676 Columbia Parkway, MS-R3, Cincinnati, OH 45226, USA. E-mail: amaynard@cdc.gov

INTRODUCTION

The past decade has seen increasing interest in nanometer-sized aerosol particles, both due to their applicability in the field of nanotechnology and due to the potential health hazard they present (Brown et al. 2000; Roco et al. 2000). Apart from the size of the particles in question, both fields are unified by the significance of interactions at the surface of particles and the need to characterize the structure, composition, and chemical activity of the particle surfaces (Donaldson et al. 1996; Lison et al. 1997; Jefferson 2000; Peukert et al. 2002). The importance of surface composition and structure becomes increasingly important at diameters of just a few nanometers as the fraction of atoms involved in surface interactions increases markedly (Preining 1998), particle stochiometry shifts from that of the bulk material and surface activity increases (Jefferson 2000).

Nanotechnology is a broad discipline concerned with the development of new technologies that utilize the unique properties of nanometer structures. Applications are wide ranging, from the formation of nanostructured materials to the development of quantum dot devices and nanomachines (Roco et al. 2000). Aerosols appear to provide a viable fabrication route in a number of cases, although the formation of nanostructure material and quantum confinement electronic devices seem to be particularly suited to using nanometer-sized aerosol particles (Maximov et al. 1993; Prost et al. 1998; Deppert et al. 1999; Kammler et al. 2001; Ostraat et al. 2001; Nanda et al. 2002). In each case, composition and structure close to the surface of the precursor particles can play a critical role in determining the properties of the final product. Understanding surface composition and structure in precursor materials is therefore important to understanding and predicting the properties of fabricated devices and materials. The ability to characterize this structure close to the surface of particles becomes increasingly

important when engineering nanoparticles with an intentional heterogeneous structure.

Research into the adverse health effects associated with exposure to nanoparticles has proceeded virtually in parallel with the development of nanotechnology, although until recently there has been little overlap between the two research areas (Borm 2002). In vivo and in vitro studies in the 1990s demonstrated that toxicologically inert materials such as polytetrafluoroethylene (PTFE) and TiO_2 appeared to become highly toxic when inhaled as nanometersized particles (Oberdörster et al. 1990, 1995). Further studies have indicated a general trend of low-solubility aerosols increasing in biological activity with increasing specific surface area (Lison et al. 1997; Oberdörster 2000; Brown et al. 2001), and it has been proposed that the inhalation toxicity of low-solubility particles is closely associated with surface area and surface chemistry but is poorly associated with the inhaled mass of material (Tran et al. 2000). While the experimental evidence appears to support this hypothesis, further validation is limited by the available information on the surface composition and chemical activity of inhaled particles.

Further investigation of the surface properties of nanoparticles and how composition and structure vary with depth from the particle surface requires analytical methods capable of probing the outer layers of individual particles. Very few analytical techniques are available that begin to approach the necessary surface sensitivity and spatial resolution. Secondary ion mass spectrometry (SIMS) and X-Ray photoelectron spectroscopy (XPS) have both been used to investigate the surface composition of micrometer-sized particles (Keyser et al. 1978; Adams and de Waele 1988; Spurny 1999). SIMS is based on the sputtering and ionization of surface atoms in an ion beam, followed by mass spectrometry, and is widely used to analyze the surface composition of materials and to investigate composition as a function of depth through extended sputtering at the analysis site. SIMS allows the outer 1–2 nm of the sample to be analyzed, although spatial resolution is generally restricted to a few 100 nm or greater (Spurny 1999). The method is therefore only applicable to the bulk analysis of collections of nanoparticles. Other surface-sensitive techniques such as X-Ray photoelectron spectroscopy (XPS) and scanning auger microscopy (SAM) have been successfully applied to surface analysis of aerosols, including welding fume (Tandon et al. 1985; Voitkevich 1988), but again are restricted by a relatively poor spatial resolution (Spurny 1999). Scanning probe microscopy techniques (including scanning tunneling microscopy (STM) and atomic force microscopy (AFM)) are surface-sensitive imaging techniques that provide nanometer spatial resolution, and in principle they can provide limited information on the surface properties of particles (Feenstra 1994; Drakova 2001; Schneider 2002). At present though, scanning probe spectrometry is not sufficiently advanced to provide a useful tool for aerosol analysis. Variable acceleration voltage energy dispersive X-ray analysis in the scanning electron microscope (SEM) has successfully been used to characterize the surface of occluded micrometer-diameter silica particles (Wallace et al. 1990; Harrison et al. 1997; Hnizdo and Wallace 2002), although the technique is inherently unsuited for nanometer-diameter particles.

Transmission electron microscopy (TEM) is widely used to characterize nanometer-sized structures and features, including aerosol particles (Maynard 2000), and it provides what is perhaps the most practical environment currently available to investigate the surface properties of nanoparticles. In the scanning operational mode (scanning transmission electron microscopy or STEM) an image is formed by displaying a detected signal as a function electron probe position. In practice, this is achieved by raster-scanning the probe over the specimen and displaying the integrated output from the detectors on a screen scanning at the same rate. The resolution of the microscope is determined by the size of the electron probe. Probes as small as 0.13 nm are achievable in microscopes such as the JEM 2010F (JEOL, Japan) used in this study, although current advances in aberration correction are anticipated to give probe sizes down to 0.05 nm in the near future (O'Keefe et al. 2001; Batson et al. 2002). The great advantage of STEM over conventional TEM is that analytical microscopy can be undertaken within a specimen volume defined by the electron beam, allowing high-resolution spatial analysis of samples. Collection of electrons that are mostly elastically scattered through high angles gives a signal that is essentially related to Rutherford scattering and provides contrast approximately proportional to the square of the atomic number of atoms within the electron beam—thus the technique's name of Z-contrast imaging (Pennycook and Boatner 1988; Hillyard et al. 1993; Jesson and Pennycook 1993; Nellist and Pennycook 1999). As high-angle scattering takes place within 0.01 nm of the atomic core, Z-contrast imaging is capable of providing semiquantitative compositional information at atomic resolution. The simplicity of image interpretation using the technique provides a significant advantage over conventional TEM techniques because key structural and compositional features of particles can be readily identified.

Energy loss analysis of electrons inelastically scattered through low angles allows simultaneous analytical spectroscopy and Z-contrast imaging with high-angle scattered electrons, providing a powerful tool for aerosol particle analysis within the STEM. Electron energy loss spectroscopy (EELS) is a well-established technique that enables local dielectric constant, charge carrier density, local atomic environment, and composition to be investigated (Egerton 1996). When used in combination with Z-contrast imaging, the electron probe can be precisely positioned at a specific point of interest within a specimen to obtain localized information (Browning et al. 1993; Duscher et al. 1998). Hydrogenic models (Allen and Rossouw 1990) show that for major energy loss features below 2 keV, atomic resolution spectroscopy is possible (Rafferty and Pennycook 1999). Energy dispersive X-ray spectroscopy (EDS) can also be used in a manner similar to EELS within the STEM, allowing compositional information to be obtained with a spatial resolution of less than

1 nm (spatial resolution is compromised in thicker specimens due to electron scattering). However, sensitivity is significantly lower than EELS for thin specimens because the effective collection angle for X-ray emissions is much smaller than that for low-angle electron scattering.

While EELS has been widely applied to the investigation of nanometer-sized structures and particles within bulk materials, there are relatively few instances of its application to aerosol particles (Maynard 1995a, 2000; Xhoffer et al. 1995; Jambers et al. 1996; Ehrman et al. 1998; Spurny 1999). The analytical capabilities of STEM at atomic spatial resolution would suggest that the technique is applicable to investigating the surface nature of ultrafine particles. A major drawback, however, is that three-dimensional (3D) structures are reduced to a two-dimensional (2D) projection in the STEM, leading to a loss of 3D information. Thus, in the general case it is hard to see how the technique could be used to quantify particle composition with depth from the surface. However, many nanoparticles approximate to spheres. Within this well-defined geometry it should be possible to infer a 3D compositional structure from a 2D analysis if there is radial symmetry. In this article we address the question of whether analysis of nanoparticles in the STEM can provide information on the compositional structure of heterogeneous particles with radial symmetry, and in particular whether the technique can be used to quantify elemental enrichment at the surface of nanoparticles. A method of relating 2D analytical information to 3D composition is developed, and an initial evaluation of its application to nanoparticles is investigated using heterogeneous welding fume particles.

THEORY

The simplest form of a heterogeneous particle with radial symmetry is perhaps a sphere with a core consisting of component Y and a shell of component X. For a given shell thickness Δr, the ratio of mass concentrations M_X/M_Y that would be seen by an electron probe placed at radial position r is predicted from simple geometrical considerations to be

$$\frac{M_X}{M_Y} = \frac{\rho_X}{\rho_Y}\left[\frac{\left(r_p^2 - r^2\right)^{\frac{1}{2}}}{\left(r_c^2 - r^2\right)^{\frac{1}{2}}} - 1\right], \qquad [1]$$

where M_X and M_Y are the mass concentrations of components X and Y, respectively; ρ_X and ρ_Y are the respective densities of the bulk materials; r is defined as radial distance from the center of the particle's projection in the x–y plane; r_p is the particle radius; and r_c is the core radius (Figure 1). Shell thickness Δr is given by $r_p - r_c$. In the idealized case of a particle exactly matching the model, Equation (1) could be used to calculate r_c from a single measurement of the concentration ratio. Of course real particles will rarely conform to such a simple model, and so a more viable approach would be to fit Equation (1) to concentration ratio measurements at a series of radial positions. This approach has the added advantage of deviations from the assumed particle structure being readily apparent in misfits between the model and the data.

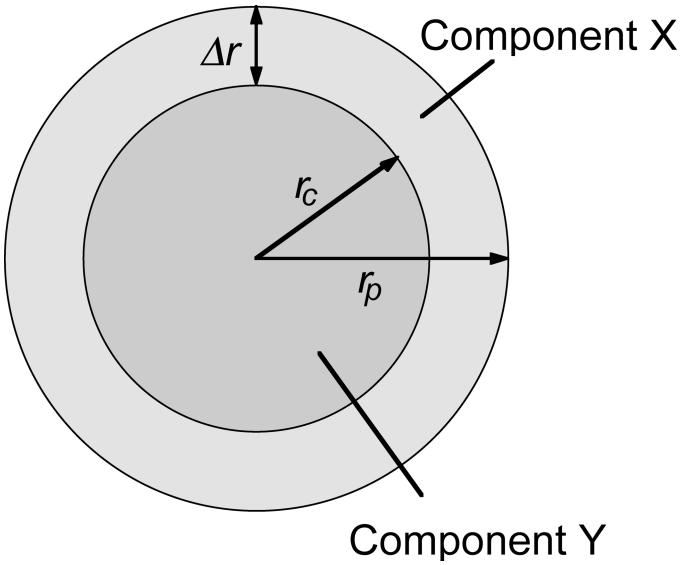

Figure 1. Schematic of an idealized particle with a simple radially symmetrical structure.

In practice, Equation (1) is too restrictive for modeling concentration values in most spherical particles exhibiting a shell structure. Even in the simple case of a core and a single outer shell, there is likely to be some mixing of components between the core and shell, resulting in Equation (1) being inapplicable. The model can be extended to deal with this additional level of complexity relatively simply. Consider the case where there is partial mixing of components X and Y in the shell and core. The volume fraction of Y in the shell is denoted by α_s and the volume fraction in the core by α_c. For convenience, the volume fraction of combined components X and Y in the shell is denoted by β_s, and in the core it is denoted by β_c. At a radial position r an electron probe would pass through thickness t_s of particle shell and thickness t_c of the core (Figure 2). When considering mixing through the particle, it is more meaningful to deal with the number of atoms of component X or Y per unit volume—denoted as C_X and C_Y, respectively—rather than mass per unit volume. While this removes the dependence on component density seen in Equation (1), accurate calculation of atomic concentration within the electron beam is still dependent on knowing the atomic number density through the particle. For simplicity, the approximation used here to estimate atomic number concentration within the electron beam effectively ignores differences in atomic number density between components, beyond what may be incorporated into the factors α and β.

At radial position r, the number concentration ratio of components X and Y can be expressed as

$$\frac{C_X}{C_Y} = \frac{\beta_s t_s + \beta_c t_c}{\alpha_s t_s + \alpha_c t_c} - 1. \qquad [2]$$

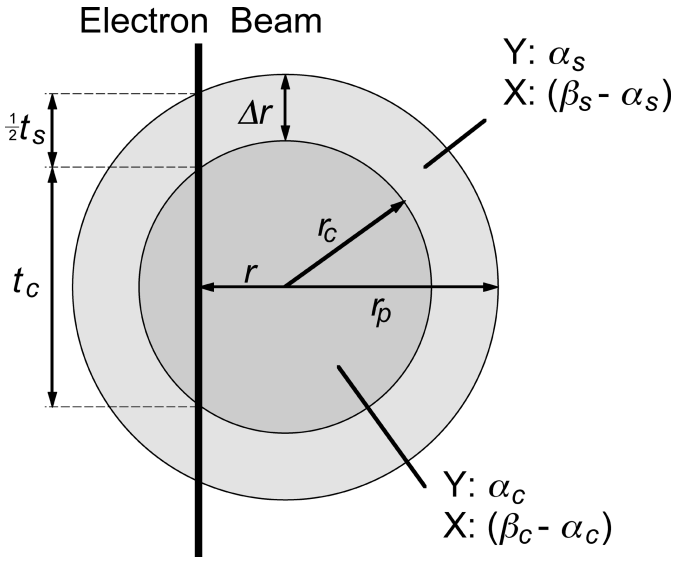

Figure 2. Schematic of a simple radially symmetrical particle with mixing of components X and Y between the core and shell.

Substituting in appropriate terms for t_s and t_c gives

$$\frac{C_X}{C_Y} = \frac{\beta_s\left(r_p^2 - r^2\right)^{\frac{1}{2}} + (\beta_c - \beta_s)\left(r_c^2 - r^2\right)^{\frac{1}{2}}}{\alpha_s\left(r_p^2 - r^2\right)^{\frac{1}{2}} + (\alpha_c - \alpha_s)\left(r_c^2 - r^2\right)^{\frac{1}{2}}} - 1. \quad [3]$$

Equation (3) has the advantage that particle structure can be modeled where the volume fractions of X and Y don't equal 1 in the shell and core, allowing for the presence of tertiary components. However, the addition of four unknown variables requires the ratio of X and Y to be measured at a minimum of five positions to enable all five parameters to be estimated.

Although it is theoretically possible to use Equation (3) to fully characterize a particle with the simple shell structure described, in practice the precision with which C_X/C_Y can be determined at small values of r is likely to affect the validity of some of the fit parameters. A further limitation arises in the accuracy with which C_X/C_Y can be determined. For the most accurate determination of C_X and C_Y measurements need to be made relative to standards of known concentration (or concentration ratio), preferably in a similar compositional environment to the particle being investigated. This is usually impractical for aerosol particles, leading to standardless analysis in most cases. Standardless analysis allows changes in concentration ratio to be measured relatively precisely, and in some cases it can provide an accurate measure of concentration ratios. However, the lack of reference to a known standard always raises a number of uncertainties regarding the absolute concentration values measured. In particular, there is often considerable uncertainty over the constant of proportionality between measured quantity and C. In simple terms, the concentration ratio C_X/C_Y can be expressed as

$$\frac{C_X}{C_Y} = k_{X,Y}\frac{N_X}{N_Y}, \quad [4]$$

where N_X and N_Y are measured quantities related to components X and Y, and $k_{X,Y}$ is the constant of proportionality between the measured ratio N_X/N_Y and the atomic number concentration ratio. For EDS analysis, k is the k-factor relating X-ray counts to elemental concentration. EELS analysis generally leads to an evaluation of atoms per unit area in the electron beam, leading to $k = 1$.

Determination of k is clearly crucial to deriving a complete particle characterization using Equation (3). However, without appropriate standards accurate determination is not always possible. Most EDS systems enable the k-factor to be estimated for a given element and emission peak within that system. Assuming that most nanometer-diameter particles can be treated as thin specimens, Equation (4) can be used directly with X-ray counts to estimate C_X/C_Y using the appropriate estimate of $k_{X,Y}$.

EELS analysis is inherently more complex than EDS, given that elemental quantification is based on ionization edges that may extend over large energy-loss intervals and result from ionization cross sections that are dependent on the atomic environment within the specimen (Egerton 1996). In general, quantification is more accurate from K and L ionization edges with relatively well-defined ionization cross sections.

To account for k, Equation (3) is more appropriately written as

$$\frac{N_X}{N_Y} = \frac{1}{k_{X,Y}}\left[\frac{\beta_s\left(r_p^2 - r^2\right)^{\frac{1}{2}} + (\beta_c - \beta_s)\left(r_c^2 - r^2\right)^{\frac{1}{2}}}{\alpha_s\left(r_p^2 - r^2\right)^{\frac{1}{2}} + (\alpha_c - \alpha_s)\left(r_c^2 - r^2\right)^{\frac{1}{2}}} - 1\right], \quad [5]$$

allowing measured quantities to be modeled directly. For Equation (5) to be a useful model for experimental data, the number of unknown variables needs to be reduced. In the case of $\beta_c = \beta_s$ (i.e., a two-component particle) the absolute value of β does not affect either the derived value of r_c or the ratio of component X to Y in the particle core or the shell. Thus, assuming this condition, an arbitrary value can be assigned to β, and useful information on the shell thickness and relative component concentrations can be obtained.

Uncertainty over the correct value of k does not affect estimates of r_c derived from fitting experimental data with Equation (5), as k simply serves to scale the function. However, the remaining unknowns are dependent on the value of k used, and if there is significant uncertainty over k modeling concentration ratios using Equation (5) are limited to just evaluating the thickness of the shell.

EXPERIMENT

The practicality of using the above method to evaluate nanoparticle structure was investigated by analyzing individual welding fume particles in the STEM. Welding fume presents a

widely recognized occupational exposure hazard (NIOSH 1988; Antonini et al. 1996, 1997), making it particularly relevant from a toxicology perspective. Particle formation from the vapor phase is predicted to lead to radial compositional structure within particles as component metals condense out at different rates, and there is limited evidence to suggest that Si surface enrichment does occur within the fume (Tandon et al. 1985; Voitkevich 1988). The fume formation process is also analogous to a number of vaporization/condensation processes used to generate nanoparticles for use in nanotechnology applications (Kammler et al. 2001; Kim et al. 2002; Singh et al. 2002; Wegner et al. 2002). This aerosol therefore provided an ideal initial test material that was relevant to both the toxicology and nanotechnology aspects of nanoparticle characterization.

Fluxless Gas Metal Arc Welding (GMAW) was carried out on a mild steel substrate within a clean air chamber (Zimmer and Biswas 2001). The fluxless alloy ER7OS-6 was used for the weld, having a composition of 97.5% Fe, 1.2–1.6% Mn, 0.8–1% Si, and 0.1% Cu. Shield gas during welding was supplied at 18 l/min and comprised 90% Ar and 10% CO_2. Fume was generated into an enclosure approximately 1 m^3 that had been previously flushed with HEPA-filtered air, resulting in a background aerosol of approximately 50 particles/cm^3 (Figure 3).

Welding and combustion fume samples have traditionally been taken using thermophoretic precipitation (Dobbins and Megaridis 1987; Maynard 1995b). However, it was found that in the experimental setup used these methods did not provide the sampling rates or degree of control desired for taking rapid samples from the plume. Instead, an alternative method of direct collection onto a TEM support grid was developed. A holder was constructed, allowing a 3 mm TEM grid to be supported while at the same time allowing air to be drawn through it. A 300 mesh lacey carbon support grid was placed in the holder, providing a matrix capable of collecting fume particles through interception and diffusion while presenting a sufficiently low flow obstacle to allow the use of a personal sampling pump to draw air through the sampler. Sampling was carried out at 0.1 l/min (Figure 3).

Prior to sampling, the sampler was removed from the vicinity of the welding area. The weld was then initiated, and the plasma arc allowed to establish. During this period, the extraction system in the enclosure was left running to remove the generated fume. Once the arc was well established, the exhaust system was switched off, and the sampling head positioned approximately 10 cm above the weld. Sampling was carried out in this position for 2 s, after which the sampler was removed and the exhaust turned back on. In this way, samples could be taken over a very short time period after the welding process had become established.

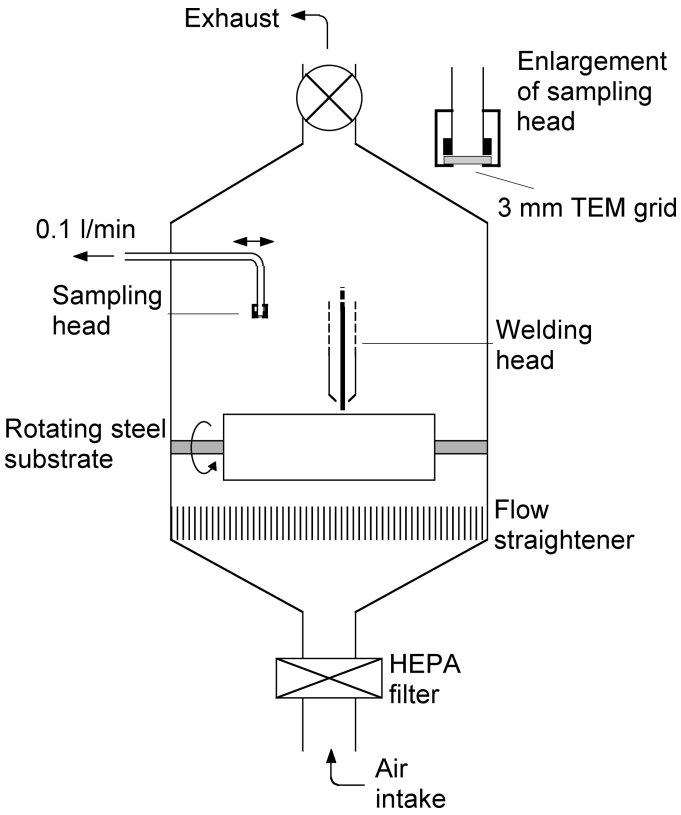

Figure 3. Schematic of the system used to generate and collect welding fume.

Sample Analysis

A JEOL JEM-2010F FasTem 200 kV field emission TEM/STEM with a Schottky field emission electron source (JEOL, Japan) was used in this work (Browning et al. 2000). The microscope was fitted with an ultrahigh resolution pole piece, which in STEM mode was capable of producing a probe size of 0.13 nm with 15 pA of current and magnifications in excess of 10,000,000×. A JEOL annular dark field detector allowed Z-contrast images in STEM mode with an imaging resolution equal to the probe size. The microscope was fitted with a piezo-driven stage to counteract specimen drift. Analytical capabilities included a Thermo Noran Vantage EDS system with a 40 mm^2 light element detector, drift compensation and spectrum imaging, and a Gatan Imaging Filter (GIF2000) which allowed EELS and energy-filtered imaging as well as spectrum imaging. A Gatan annular dark field detector placed before the GIF allowed simultaneous imaging and analysis using EELS. For EDS a spatial resolution of around 1 nm was possible while still having enough beam current to generate sufficient X-rays for analysis, and for EELS a resolution of 0.2 nm was possible.

Particles within the sample were initially imaged using bright-field TEM and annular dark field STEM imaging. The aerosol was typical of welding fume, comprised of long–chain-like agglomerates. Primary particles forming the agglomerates appeared to fall into two predominant categories—particles approximately 5–10 nm in diameter and spherical particles around 50–150 nm in diameter (Figure 4). Particles in the 50–150 nm category were selected for further analysis. TEM images of individual particles indicate a core/shell structure (Figure 5),

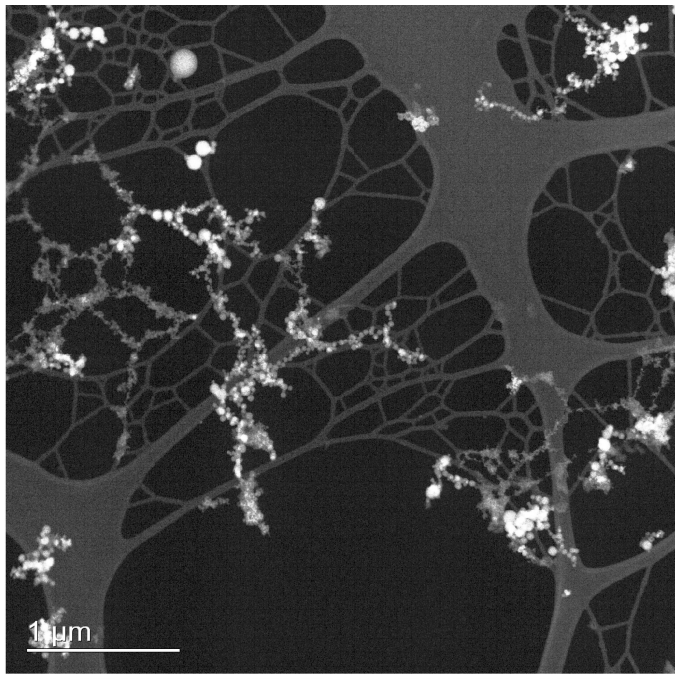

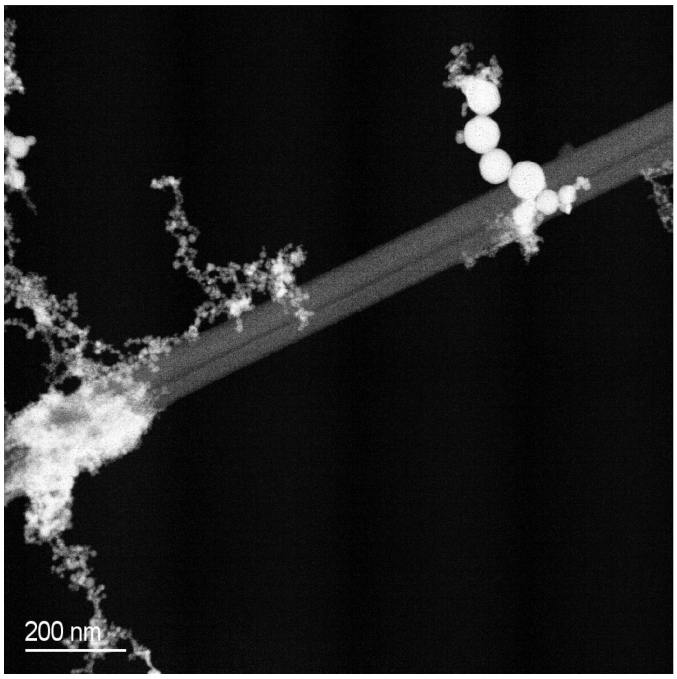

Figure 4. STEM annular dark field images of collected welding fume, showing the presence of two distinct types of primary particle.

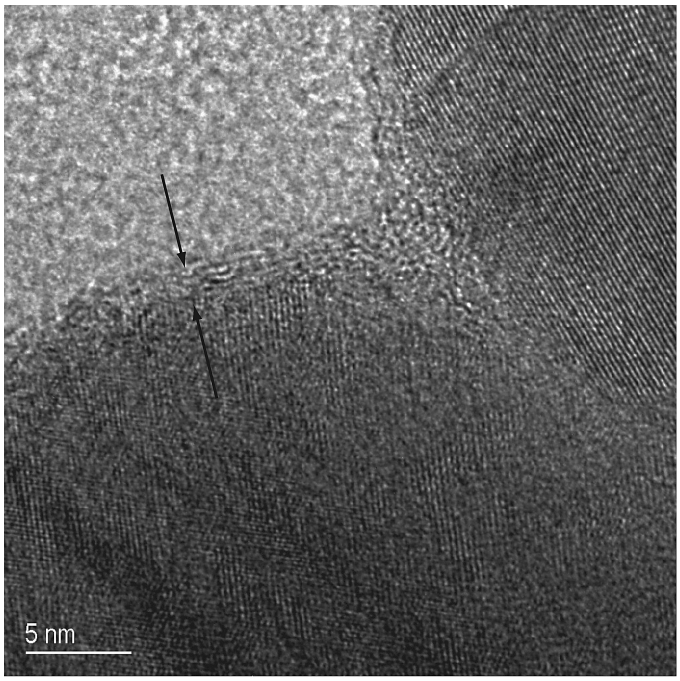

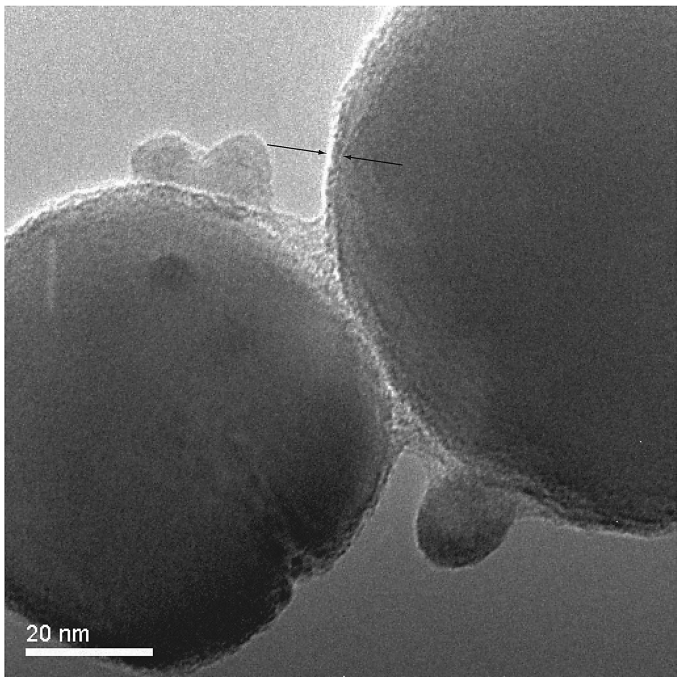

Figure 5. Conventional TEM images, showing the presence of a thin outer shell-like structure around larger welding fume primary particles. Lattice fringes are apparent in the top image, showing the core of the particle to be crystalline.

although determination of the shell thickness or composition was not directly possible.

Energy-filtered imaging (Crozier 1995) was also used with the microscope in STEM mode to qualitatively determine the presence of Si enrichment at the surface of particles. Images were acquired using electrons forming the Fe M ionization edge and the Si L edge. By dividing the Si image by the Fe image, it was possible to qualitatively identify regions with particularly high Si content. Although image intensity using this method is influenced by a number of factors, it does allow regions where there is an abrupt change of elemental composition to be identified. Many particles imaged show no clear evidence of high Si concentration at the edge of particles, although in

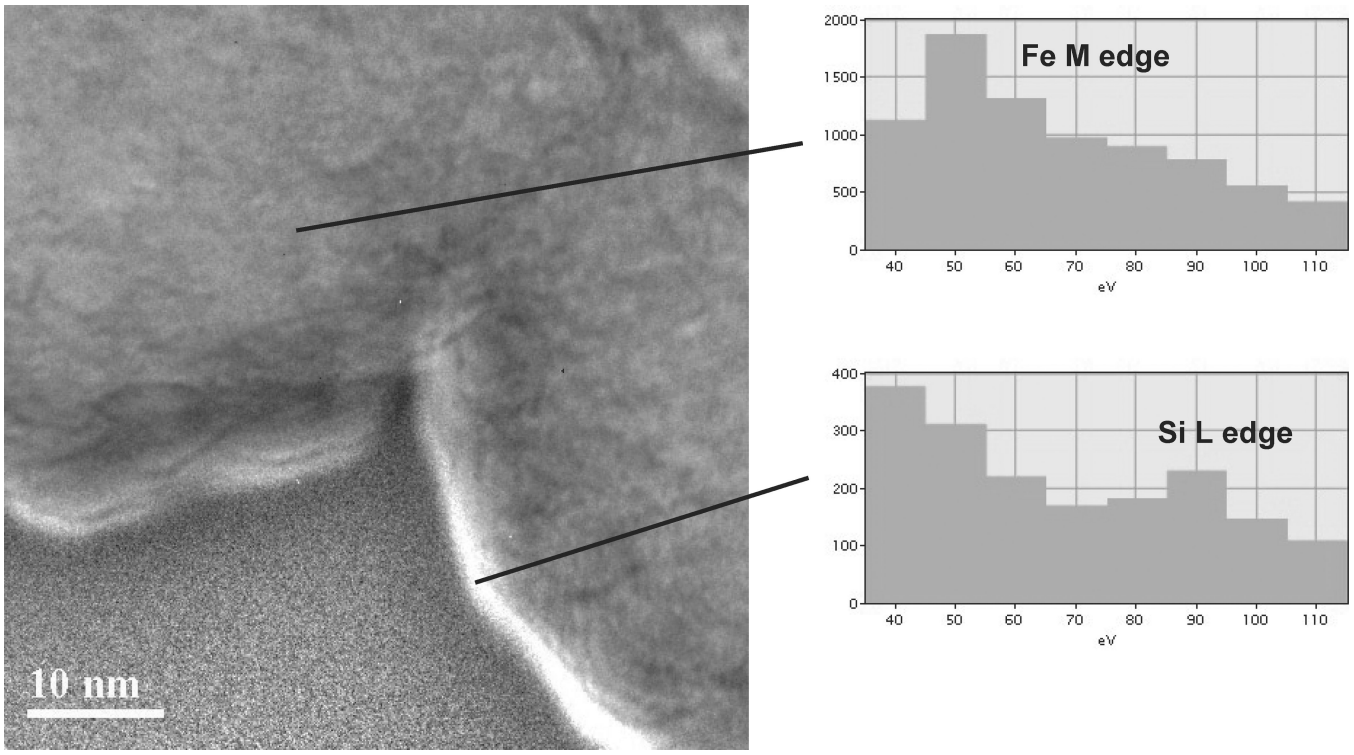

Figure 6. Energy-filtered image of the edge of two adjoining particles, indicating a region of high Si content (bright feature).

some cases there was a clear indication of Si enrichment at the surface (Figure 6). The technique is limited by long data acquisition times, and thus in many cases it was unclear whether the lack of observed Si enrichment was associated with the particle structure or damage/drift during data acquisition.

Two particles showing a clear Si signature were selected for detailed EDS and EELS analysis. Both of these particles were greater than 100 nm in diameter and thus were technically outside the ultrafine particle region. However, the analysis method is not strongly dependent on absolute particle diameter as long as there is a low rate of multiple electron scattering within the particle (i.e., the particle represents a thin specimen). Under the analysis conditions used, the electron inelastic scattering mean free path (λ_e) will typically be greater than 80 nm (Egerton 1996). At most sampling points, specimen thickness was less than or comparable to Λ_e, allowing the thin-specimen approximation to be used. A series of EDS spectra were collected from the particle shown in Figure 7 using an electron probe diameter of approximately 0.5 nm, and a collection time of typically 60 s. Collection time was limited by the onset of specimen damage, and even after 60 s degradation of the sample was visible around the site of the electron beam. Analysis points ranged between 2 nm and 52 nm from the edge of the imaged particle, giving effective specimen thicknesses between 35 nm and 147 nm (assuming a spherical particle). Detailed EELS analysis was carried out on the particle shown in Figure 8. A beam width of 0.2 nm was used, and spectra were acquired at a range of radial positions using collection times between 3 and 6 s. Analysis points ranged between 1.5 nm and 4.5 nm from the edge of the imaged particle, giving effective specimen thicknesses between 28 nm and 49 nm, assuming a spherical particle. Spectra were acquired with a channel width of 0.2 eV, and a full width half maximum value of 1.2 eV. The resulting spectrum width of 204 eV allowed simultaneous collection of Fe M and Si L ionization edges, but not the Fe L edge. Mn L and O K edges could also be acquired simultaneously, but not at the same time as an appropriate Fe or Si edge. The Fe M edge is not ideally suited to quantitative analysis due to its extended structure and uncertainty over the scattering cross section. To allow comparison between the O K, Si L, and Fe L edges, separate spectra were collected for each respective energy loss region. As the particle had a tendency to degrade under the electron beam, spectra associated with each ionization edge were acquired from different regions around the edge of the particle (Figure 8). Elemental ratio as a function of radial distance from the center of the particle was estimated using linear interpolation when comparing edges not acquired at the same time.

RESULTS

TEM images of particles between 50 and 150 nm in diameter indicated the presence of an outer shell approximately 1–2 nm thick (Figure 5). The shell led to lower image contrast than the particle cores, and appeared to be amorphous in structure.

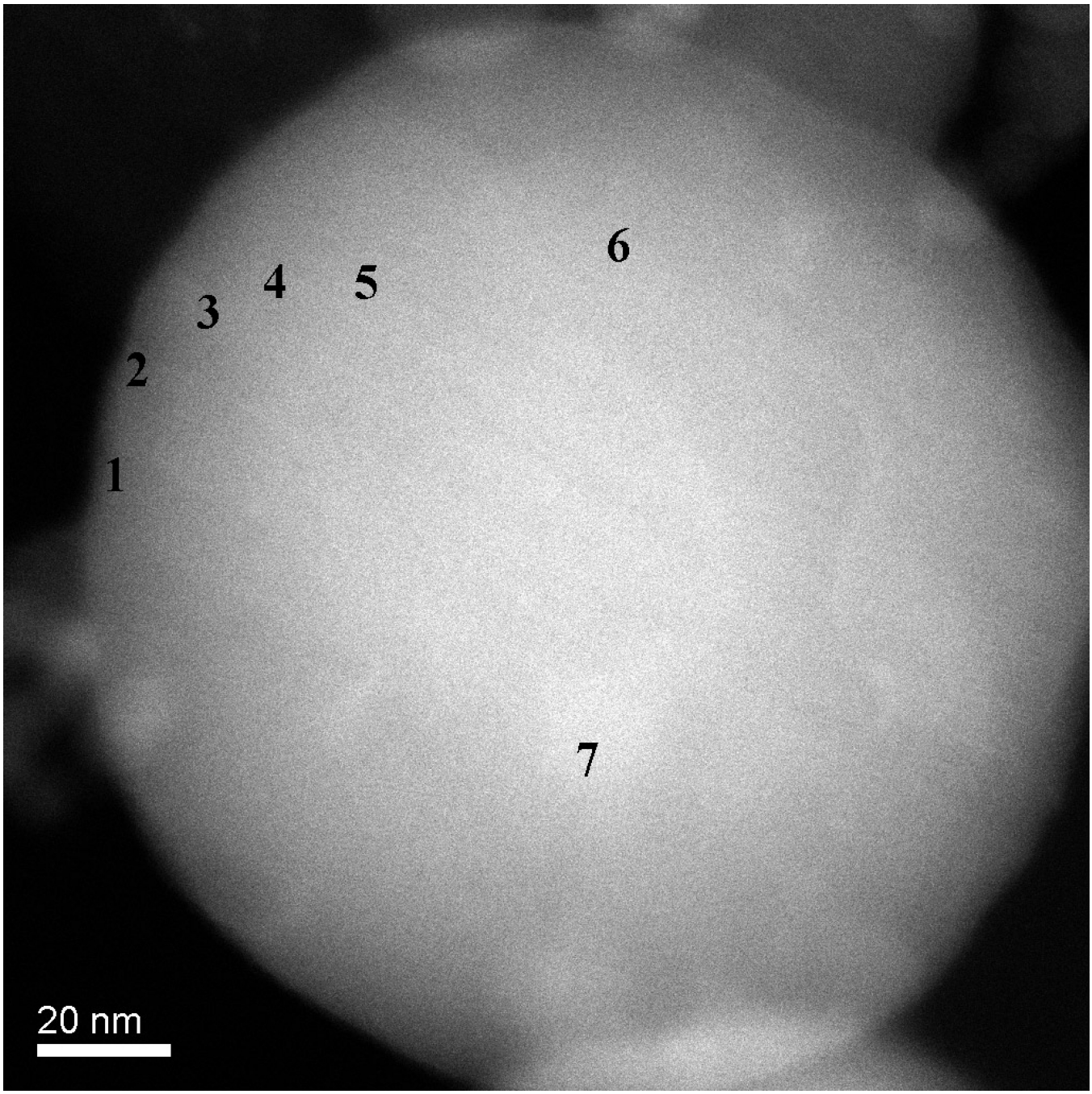

Figure 7. STEM annular dark field image of a welding particle characterized using EDS. Analysis was carried out at the points shown using a 0.5 nm diameter electron beam and with acquisition times typically of 60 s.

Energy-filtered imaging qualitatively indicated an outer Si-rich shell in some cases that was possibly between 1–3 nm thick (Figure 6). However, there was a high degree of variability within particles of the same size range. EDS analysis indicated that the Si content of the particles was highly variable, with a number of particles examined having no detectable Si component. Even in many particles that were relatively rich in Si, the relatively poor sensitivity of EDS analysis didn't allow the routine identification of Si enrichment at the particle's surface. EELS analysis confirmed the variability in Si content. Qualitative indication of Si surface enrichment was possible by positioning the electron probe precisely at the particle surface using the high-angle coherent convergent beam diffraction pattern, or Ronchigram (Cowley 1986; James and Browning 1999) (when the electron probe is

Figure 8. STEM annular dark field image of welding particle used in EELS analysis. Analysis was carried out in the regions shown using a 0.2 nm diameter electron beam and with acquisition times between of 3 and 6 s.

focused on the specimen, the center of the resultant Ronchigram exhibits infinite magnification, and is thus a very sensitive tool for finding the edge of a specimen). In many cases, a marked increase in the Si L edge and a corresponding decrease in the Fe M edge was observed at the extreme edge of particles. This analysis approach proved useful in identifying particles with Si surface enrichment, but did not lend itself to characterizing the thickness or composition of the shell. Figure 9 shows EELS data from the edge of a 5 nm particle, qualitatively demonstrating an increase in the Si/Fe ratio at the very edge of the particle. The exponentially decreasing EELS spectrum background has been removed from the spectra to show the Fe $M_{2,3}$ and Si $L_{2,3}$ excitation edges, and the spectra offset to aid comparison. In each of the spectra, the area under the Si $L_{2,3}$ edge is approximately constant, indicating similar atomic concentrations of Si in the electron beam at each point. The increasing area under the Fe

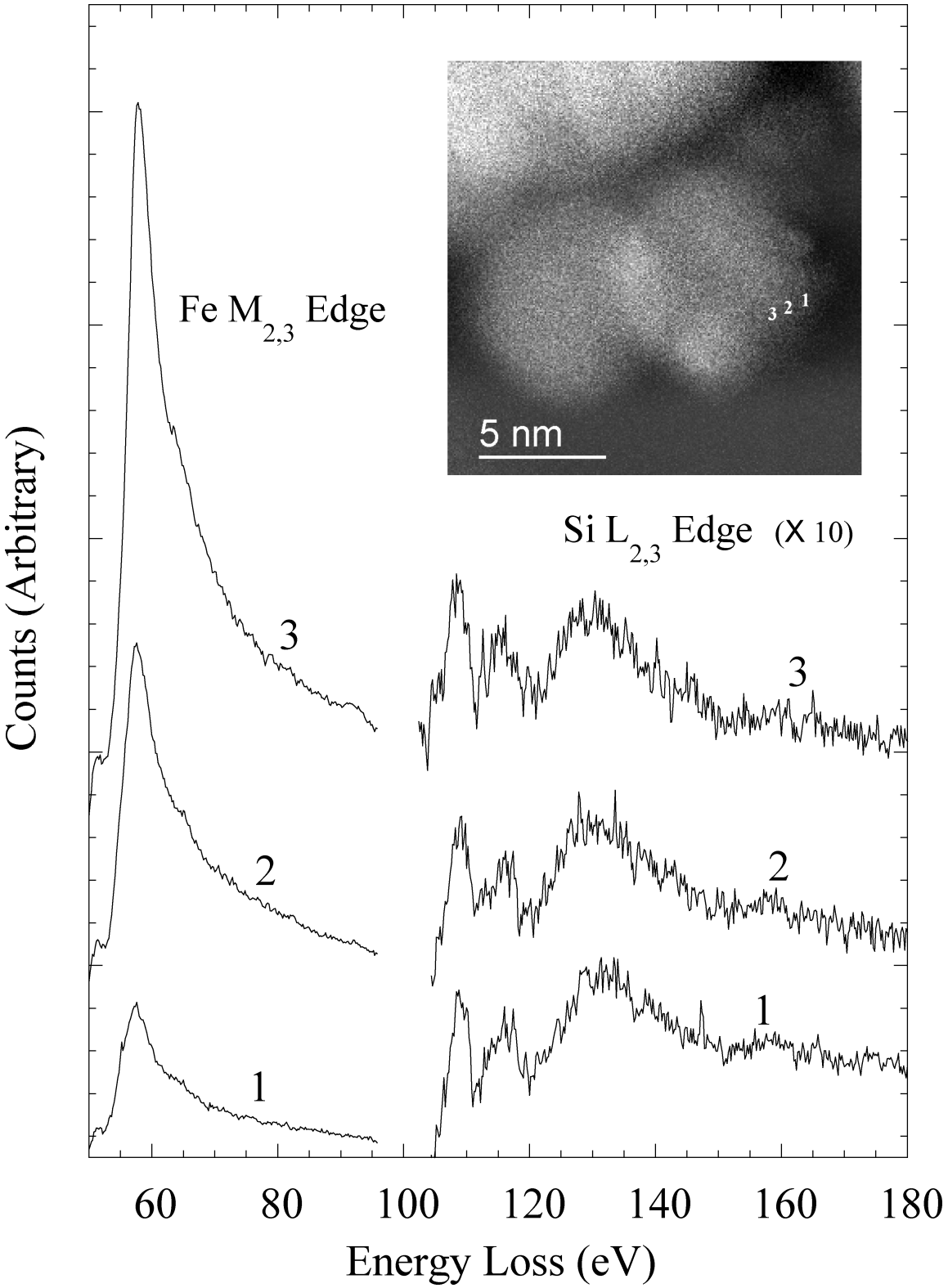

Figure 9. EELS spectra from the edge of a 5 nm particle. The exponentially decreasing energy-loss background has been removed from both edges shown, allowing qualitative comparison of the Si/Fe ratio with analysis position. Spectra from positions 1–3 are vertically offset to allow easier comparison.

$M_{2,3}$ edge as the analysis point moves closer to the center of the imaged particle indicates an increase in Fe concentration; the decreasing Si/Fe ratio away from the imaged particle's edge is consistent with an outer region of Si enrichment.

Two particles were selected for detailed analysis using EDS and EELS (Figures 7 and 8 respectively). The particles were 156 nm and 133 nm in diameter, respectively, although the analysis depths towards the edge of the particles were of the order of tens of nm. Figure 10 shows Si/Fe X-ray count ratio and Mn/Fe count ratio as a function of radial distance from the particle image's center (Figure 7) using EDS analysis. Measurement errors are based on Poisson count errors. Appropriate k-factors were used to convert from X-ray counts to atomic number concentrations. A clear increase in Si concentration compared to Fe is seen in the particle, whereas Mn appears to match Fe concentration throughout the particle. The data were fitted using Equation (5) and nonlinear regression using the software package *Mathematica*® (Wolfram, USA), assuming $\beta_s = \beta_c = 1$. The resulting fits, together with the fit parameters and estimated shell thickness, are shown in Figure 10.

Data from the analysis of the particle in Figure 8 using EELS is shown in Figure 11. Elemental ratio in terms of atoms per unit area is plotted against radial distance from the particle image's center in each case. Ratios for the Si L edge to Fe M edge and O K edge to the Mn L edge are from the same analysis points on the particle. In all other cases, linear regression was used to estimate concentration ration with radial position. Data points were plotted with a nominal $\pm 20\%$ error, giving a rough estimate of the error associated with the EELS analysis. The data were fitted using Equation (5) and nonlinear regression as for the EDS data, assuming $\beta_s = \beta_c = 1$. The resulting fits, together with the fit parameters and estimated shell thickness, are shown in Figure 11. Error associated with the fit parameters has been estimated from the nonlinear regression and also from uncertainty over radial position within the particle. The results show Si to be enriched at the surface of the particle with respect to Fe, although there is a large discrepancy between the Si/Fe concentration measured using the Fe M edge and the Fe L edge. O is also seen to be enriched at the particle surface with respect to Fe, as is Mn, whereas O is indicated as remaining relatively constant with respect to both Si and Mn.

DISCUSSION

Both the EDS and EELS data presented demonstrate that elemental surface enrichment can be observed in nanometer-sized particles. EDS offers perhaps the most accurate means of quantifying the thickness of the enrichment layer, and the degree of enrichment, although accuracy is somewhat limited without appropriate standards. However, the technique is relatively insensitive, leading to long acquisition times and the increased possibility of specimen damage or contamination occurring during the analysis. Although it was possible to quantify elemental composition at positions 1 and 2 in Figure 7, it is unlikely that sufficient measurement precision would be possible from thinner sample sections within the 60 s acquisition time. The particle thickness at these points was around 35 nm. As a rough estimate, using the same measurement parameters, it is unlikely that EDS could be used to quantify the thickness and composition of surface shells less than a few nm thick on particles smaller than 70–80 nm in diameter. Sensitivity could be improved through the use of larger X-ray collection angles, and the use of a cold-stage to reduce specimen damage and drift over long acquisition times.

As expected, EELS offered substantially greater sensitivity over EDS. In the analyses carried out EELS consistently provided more detailed information on particle composition at a (sample volume $\times$ acquisition) factor between 60 and 120 times smaller than that for EDS. Figure 9 demonstrates the ability of EELS to extract information from very small particles. The analysis depth at point 1 is approximately 1 nm, and the Fe M and Si L edges are clearly distinguishable, indicating that using EELS to investigate surface enrichment could successfully be applied to particles approaching 1–2 nm in diameter.

Despite the clear advantages of EELS, it is limited by uncertainty in quantification of ionization edges and by the need to acquire data in different regions of the energy loss spectrum sequentially. It is also practically limited to the analysis of lighter elements. Limiting quantification to K and L ionization edges effectively restricts analysis to elements of atomic number 37 (Ruthenium) and lower within a 0–2000 eV energy loss range. Quantification using M edges is possible but difficult due to uncertainties over scattering cross section. In the case of M edges in the low-loss region (typically less than 100 eV) quantification is also limited by the presence of plasmon peaks from bulk electron excitations. The difficulties of using M edges is demonstrated in the EELS ratios for Si L/Fe M and Si L/Fe L (Figure 11). Although both ratios as a function of radial position demonstrate surface enrichment of Si, the Si/Fe ratio using the Fe M edge is approximately ten times lower than that using the L edge. This is most likely due to errors associated with quantifying Fe concentration using the M edge. Assuming that the Si/Fe ratio using the Fe M edge is related to the actual ratio by a constant factor (k in Equation (5)), modeling the data with Equation (5) should lead to the correct value of Δr. Δr estimated using the Fe L and Fe M edges differs by 0.58 nm, indicating that use of the Fe M edge may be used to approximate the shell thickness. Closer examination of Fe concentration derived from the Fe M and Fe L edges shows the estimated elemental concentrations to diverge increasingly towards the center of the particle. This is commensurate with the idea that quantification of the M edge is affected by the presence of plasmons (the intensity of which is associated with specimen thickness), and goes some way to explaining the discrepancy between Δr estimated using the L and M edges.

EELS analysis indicated a surface shell around the particle in Figure 8 approximately 1 nm thick with elevated concentrations of Si, O, and Mn. The shell thickness is similar to that observed

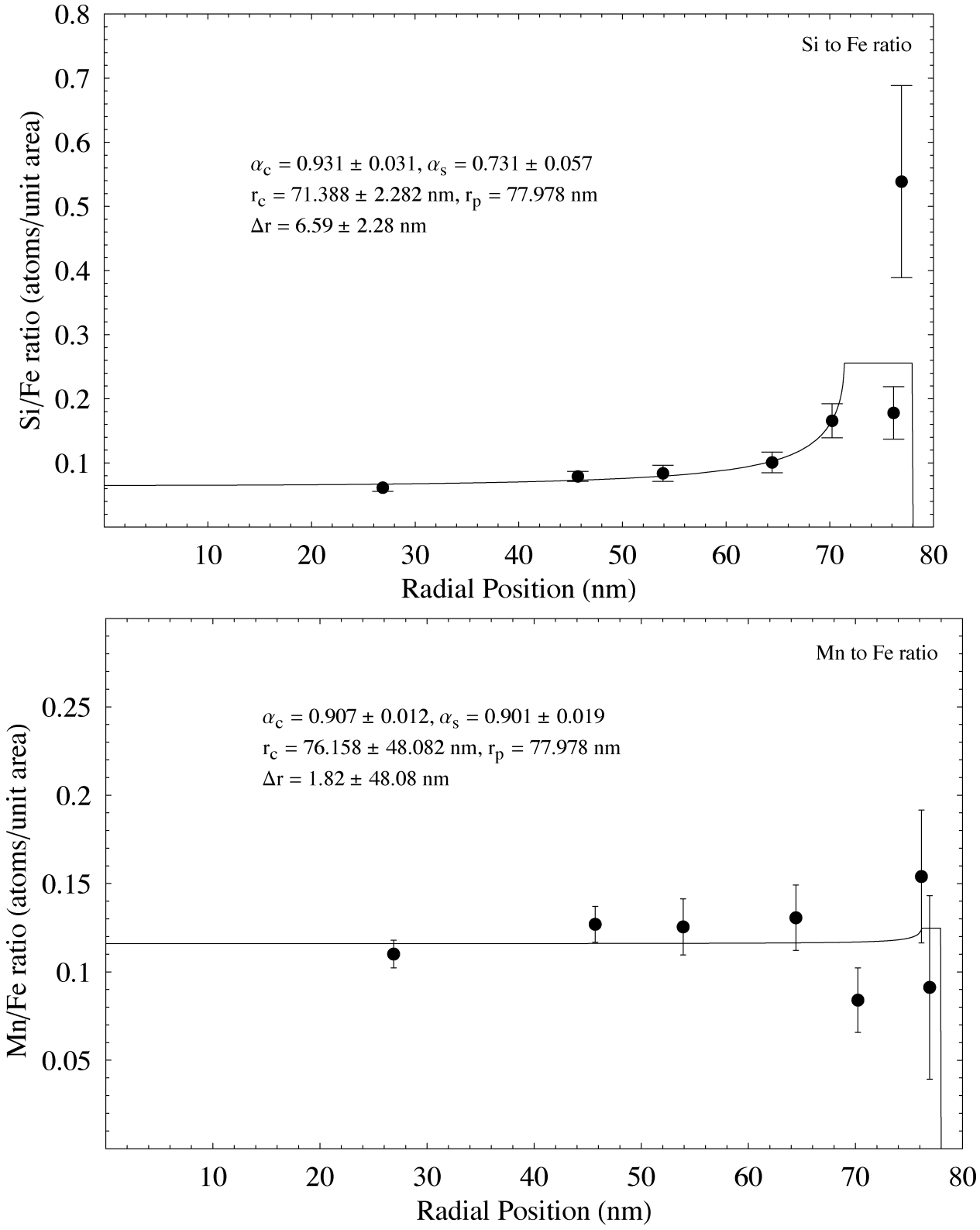

Figure 10. Elemental ratio (X-ray counts) as a function of radial distance for the particle shown in Figure 7, measured using EDS analysis. Equation (5) has been fit to the data using nonlinear regression to estimate the various model parameters and shell thickness λr. In each case λ_c and λ_s have been assigned nominal values of 1. Estimated parameter errors are the standard error from the nonlinear regression.

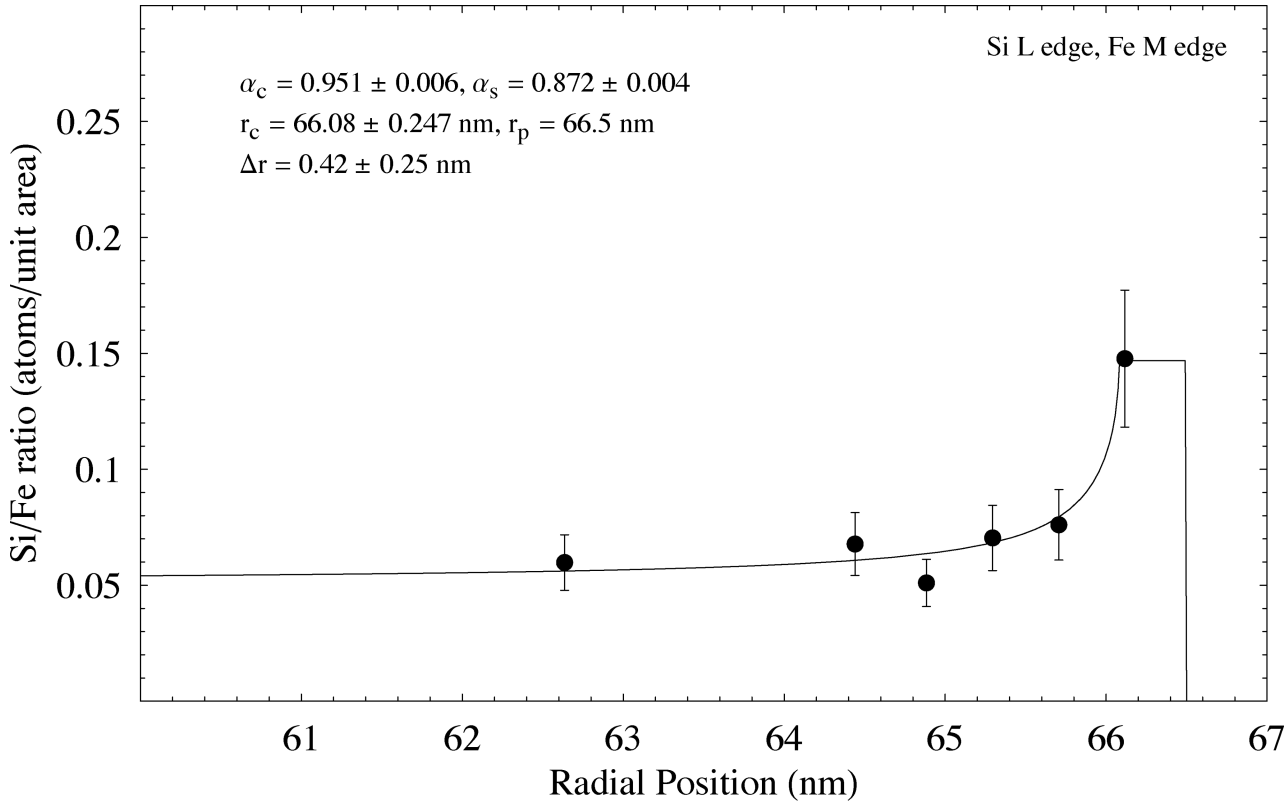

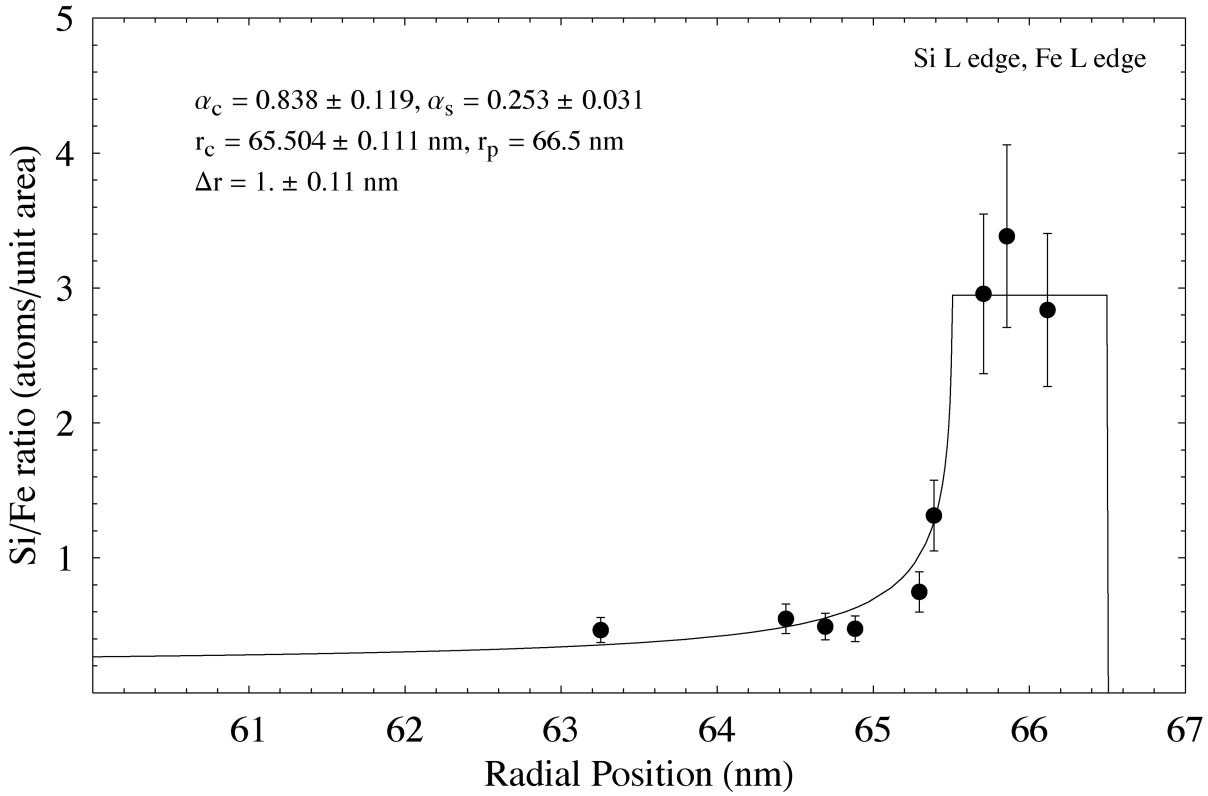

Figure 11. Elemental ratio (atoms per unit area) as a function of radial distance for the particle shown in Figure 8 measured using EELS analysis. Equation (5) has been fit to the data using nonlinear regression to estimate the various model parameters and shell thickness λr. In each case λ_c and λ_s have been assigned nominal values of 1. Estimated parameter errors are associated with uncertainty over radial position, and the model fit. Data points are shown with an estimated ± 20% error. (*Continued*)

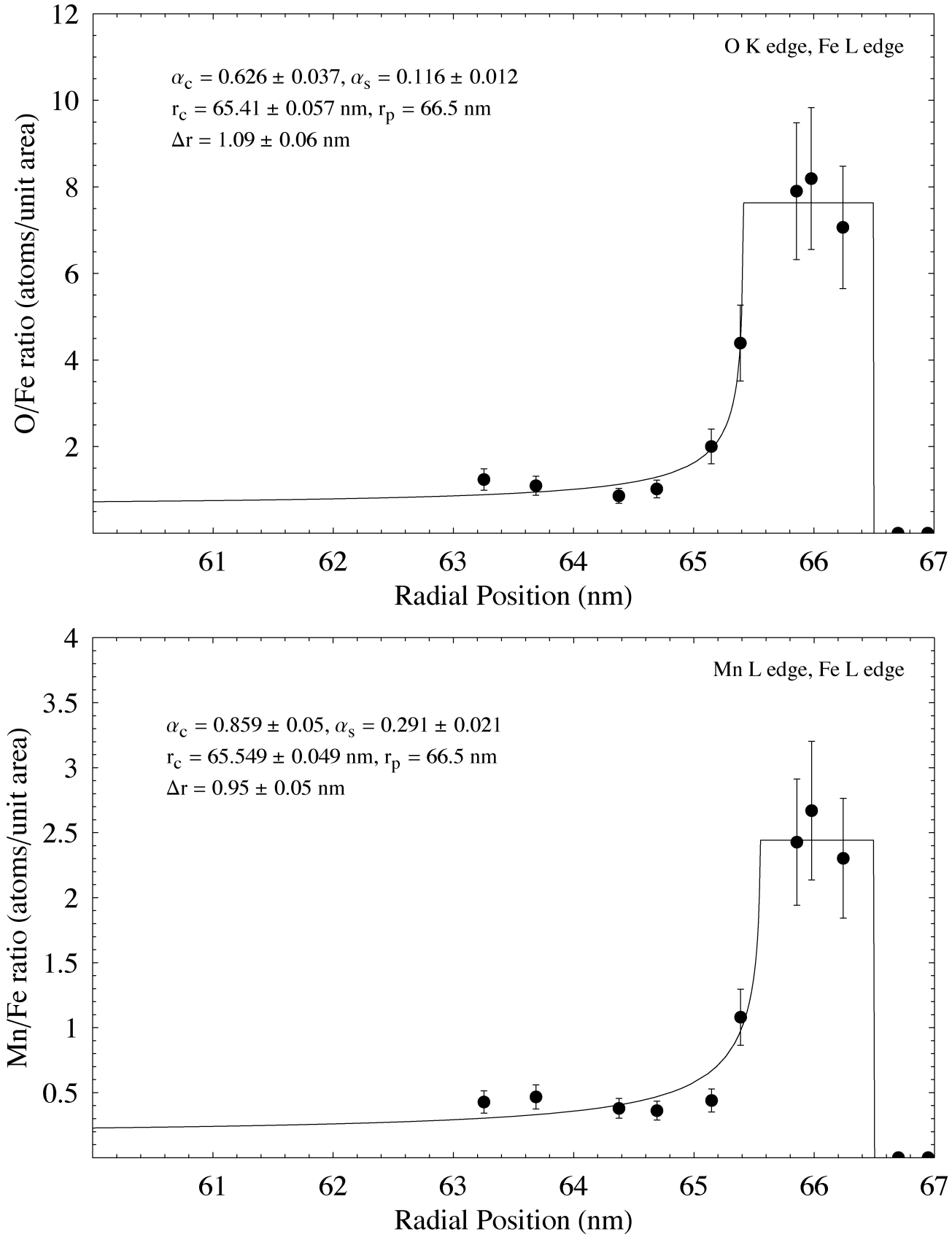

Figure 11. (Continued)

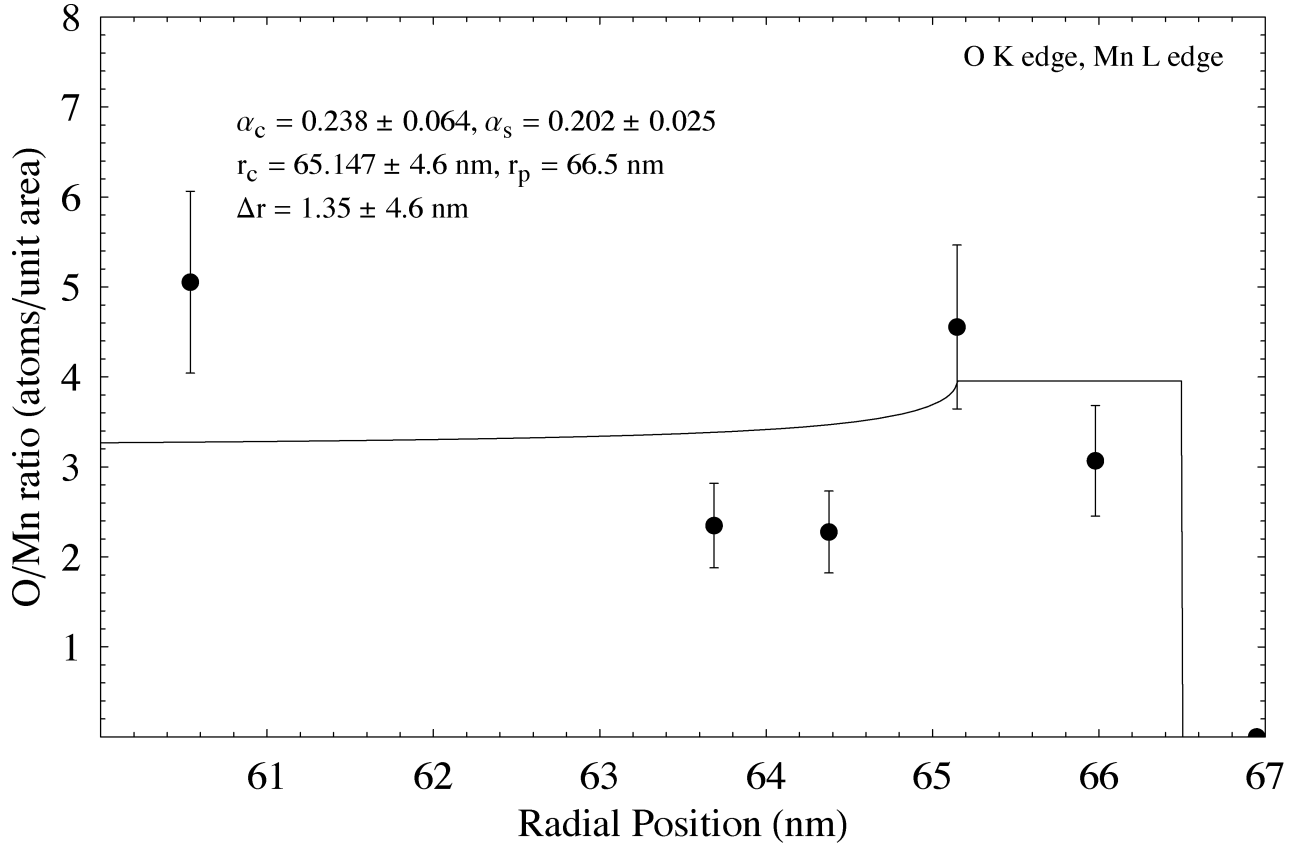

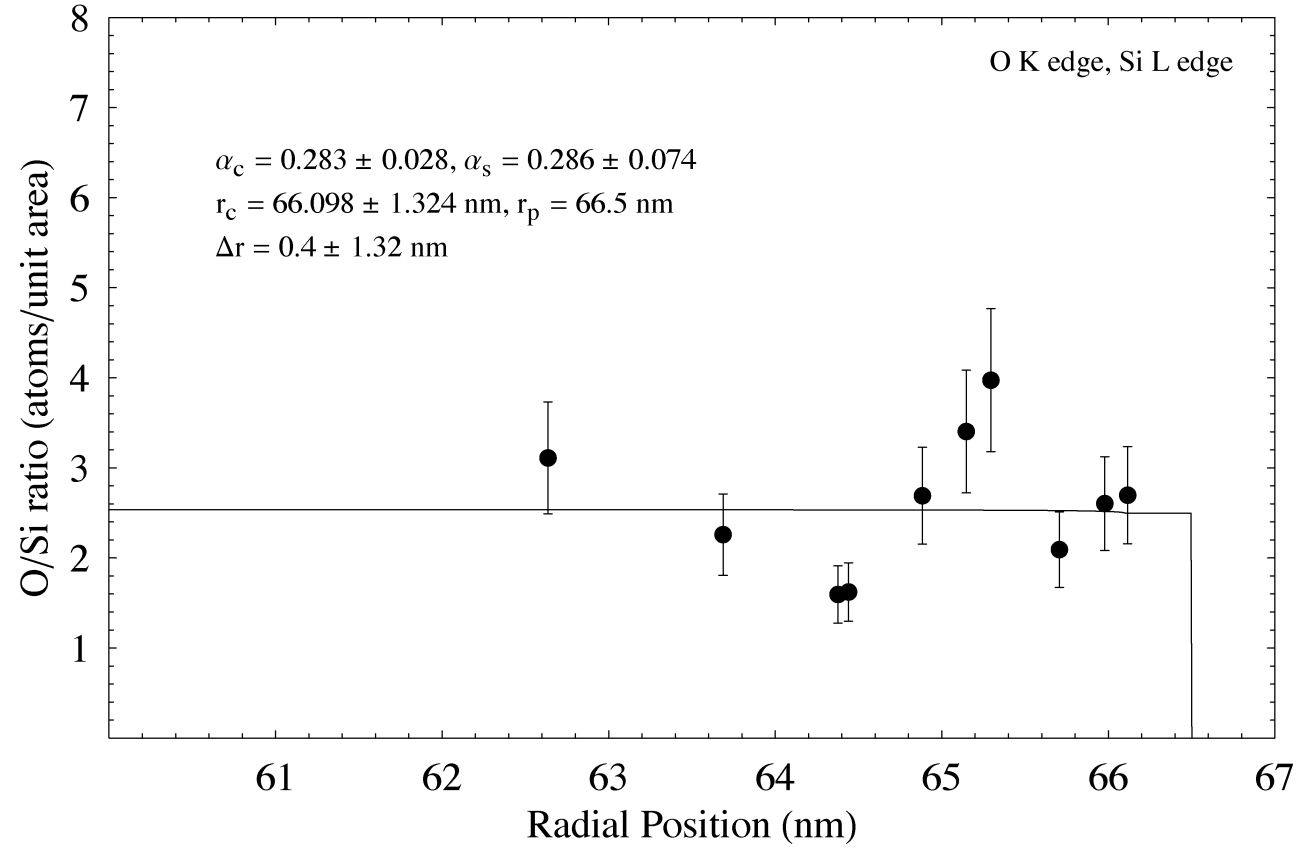

Figure 11. (Continued)

qualitatively in other particles of similar size using TEM imaging and energy-filtered imaging (Figures 5 and 6). Estimates of Δr are insufficiently accurate to determine whether the shells associated with the different elements are of different thicknesses. EDX analysis on a similar particle indicated a much thicker, Si-rich shell of 6.6 nm (Figure 10), although the model doesn't fit the data well at high radii—possibly due to local variations in concentration around the edge of the particle, or possibly due to the uncertainty of EDS measurements with such a thin specimen. Surface enrichment of Si in some particles confirms the findings of previous macroscopic studies on welding fume (Tandon et al. 1985; Voitkevich 1988). Interestingly, the EDS analysis indicates no surface enrichment of Mn, whereas the EELS analysis does (Figures 10 and 11). Although from a metallurgical viewpoint Mn would be expected to form a matrix with Fe during the particle formation process (Voitkevich 1988), these measurements indicate that Mn may preferentially condense on the outside of particles in some cases.

Further examination of the EELS data indicates the outer shell to be dominated by oxygen. Data suggest approximate core and surface stochiometries of SiO_3MnFe_5 and $Si_6O_{16}Mn_5Fe_2$, respectively. Although the presence of clear compounds is not obvious, it is reasonable to surmise that a significant fraction of the particle shell is comprised of oxides (as would be expected). The decrease in Fe with respect to Si and Mn is indicative of these elements condensing out of the vapor phase at a later time than the Fe, and gives a possible insight into the time–temperature history of the particle. Both the Si/Fe and Mn/Fe ratios in the particle core are higher than in the welding alloy, suggesting that variation in elemental composition would be expected between individual particles.

In order to simplify the nonlinear fit process, β_c and β_s were assumed to be equal in all analyses. Limited investigation of fitting the data with Equation (5) to determine all five unknown parameters indicated that the quality of the data was too poor to allow the identification of unique solutions without assuming values for β. Observing the data in Figures 10 and 11 it is clear that assuming equal values of β in the particle core and shell is not valid, as the particle clearly has multiple elemental components. Inspection of Equation (5) would indicate that small differences between β_c and β_s would not greatly affect the derived values of r_c, α_c, and α_s. However, further research is required to determine how far assumptions on β can be taken and the quality of data necessary to determine all five parameters accurately.

SUMMARY

Assuming a simple shell structure and applying Equation (5) to EDS and EELS data has allowed us to successfully quantify the compositional structure of selected welding fume particles. Although at this stage we don't have sufficient information to comment on the accuracy of the derived parameters, this approach would appear to be a useful tool to examine surface enrichment within spherical nanoparticles. Further research should establish the accuracy of the approach and whether it can be successfully extended to more complex particle structures, particularly with the advent of subangstrom resolution analytical electron microscopy (O'Keefe et al. 2001; Batson et al. 2002). The ability to characterize the surface of radially symmetrical particles in this manner should allow a better understanding of the formation of nanoparticles from the vapor phase to be established, particularly with regards to studying the time–temperature history of subsets of particles. The information obtained will be of benefit to nanotechnologies using nanoparticle precursors and also to the understanding of the formation of aerosols detrimental to health, such as welding fume. Applying the technique to occupational and ambient aerosols will also provide necessary information on the surface nature of low-solubility particles, and how this may impact on the toxicity of those particles in the lungs.

REFERENCES

Adams, F., and de Waele, J. (1988). Surface Analysis in Atmospheric Environmental Studies, *Surf. Int. Analysis* 12:551–564.

Allen, L. J., and Rossouw, C. J. (1990). Absorptive Potentials Due to Ionization and Thermal Diffuse-Scattering by Fast Electrons in Crystals, *Phys. Rev. B* 42(18):11644–11654.

Antonini, J. M., Murthy, G. G. K., and Brain, J. D. (1997). Responses to Welding Fumes: Lung Injury, Inflammation, and the Release of Tumor Necrosis Factor-Alpha and Interleukin-1 Beta, *Exper. Lung Res.* 23(3):205–227.

Antonini, J. M., Murthy, G. G. K., Rogers, R. A., Albert, R., Ulrich, G. D., and Brain, J. D. (1996). Pneumotoxicity and Pulmonary Clearance of Different Welding Fumes after Intratracheal Instillation in the Rat, *Toxicol. Appl. Pharmacol.* 140(1):188–199.

Batson, P. E., Dellby, N., and Krivanek, O. L. (2002). Sub-angstrom Resolution Using Aberration Corrected Electron Optics, *Nature* 418(6898):617–620.

Borm, P. J. A. (2002). Particle Toxicology: From Coal Mining to Nanotechnology, *Inhalation Toxicol.* 14(3):311–324.

Brown, L. M., Collings, N., Harrison, R. M., Maynard, A. D., and Maynard, R. L. (2000). Ultrafine Particles in the Atmosphere: Introduction, *Phil. Trans. Royal Soc. London Series A-Math. Phys. Eng. Sci.* 358(1775):2563–2565.

Brown, D. M., Wilson, M. R., MacNee, W., Stone, V., and Donaldson, K. (2001). Size-Dependent Proinflammatory Effects of Ultrafine Polystyrene Particles: A Role for Surface Area and Oxidative Stress in the Enhanced Activity of Ultrafines, *Toxicol. Appl. Pharmacol.* 175(3):191–199.

Browning, N. D., Chisholm, M. F., and Pennycook, S. J. (1993). Atomic-Resolution Chemical-Analysis Using a Scanning-Transmission Electron-Microscope, *Nature* 366(6451):143–146.

Browning, N. D., James, E. M., Kishida, K., Arslan, I., Buban, J. P., Zaborac, J. A., Pennycook, S. J., Xin, Y., and Duscher, G. (2000). STEM an Experimental Tool for Atomic Scale Interface Science, *Rev. Adv. Mat. Sci.* 1:1–26.

Cowley, J. M. (1986). Electron Diffraction Phenomena Observed with a High Resolution STEM Instrument, *J. Elect. Microsc. Technique* 3:25–44.

Crozier, P. A. (1995). Quantitative Elemental Mapping of Materials by Energy-Filtered Imaging, *Ultramicroscopy* 58(2):157–174.

Deppert, K., Bovin, J. O., Magnusson, M. H., Malm, J. O., Svensson, C., and Samuelson, L. (1999). Aerosol Fabrication of Nanocrystals of InP, *Jpn. J. Appl. Phys. Part A* 38(2B):1056–1059.

Dobbins, R. A., and Megaridis, C. M. (1987). Morphology of Flame-Generated Soot as Determined by Thermophoretic Sampling, *Langmuir* 3:254.

Donaldson, K., Beswick, P. H., and Gilmour, P. S. (1996). Free Radical Activity Associated with the Surface of Unifying Factor in Determining Biological Activity? *Toxicol. Lett.* 8(1–3):293–298.

Drakova, D. (2001). Theoretical Modelling of Scanning Tunnelling Microscopy, Scanning Tunnelling Spectroscopy and Atomic Force Microscopy, *Rep. Prog. Phys.* 64(2):205–290.

Duscher, G., Browning, N. D., and Pennycook, S. J. (1998). Atomic Column Resolved Electron Energy-Loss Spectroscopy, *Phys. Status Solidi A-Appl. Res.* 166(1):327–342.

Egerton, R. F. (1996). *Electron Energy-Loss Spectroscopy in the Electron Microscope*. 2nd ed. Plenum Publishing Corporation, New York.

Ehrman, S. H., Friedlander, S. K., and Zachariah, M. R. (1998). Characteristics of SiO2/TiO2 Nanocomposite Particles Formed in a Premixed Flat Flame, *J. Aerosol. Sci.* 29(5–6):687–706.

Feenstra, R. M. (1994). Scanning Tunneling Spectroscopy, *Surf. Sci.* 300(1–3):965–979.

Harrison, J., Brower, P., Attfield, M. D., Doak, C. B., Keane, M. J., and Wallace, W. E. (1997). Surface Composition of Respirable Silica Particles in a Set of US Anthracite and Bituminous Coal Mine Dusts, *J. Aerosol Sci.* 28:689–696.

Hillyard, S., Loane, R. F., and Silcox, J. (1993). Annular Dark-Field Imaging—Resolution and Thickness Effects, *Ultramicroscopy* 49(1–4):14–25.

Hnizdo, V., and Wallace, W. E. (2002). Monte Carlo Analysis of the Detection of Clay Occlusion of Respirable Quartz Particles Using Multiple Voltage Scanning Electron Microscopy, *Scanning* 24(5):264–269.

Jambers, W., DeBock, L., and VanGrieken, R. (1996). Applications of Micro-Analysis to Individual Environmental Particles, *Fresenius J. Anal. Chem.* 355(5–6):521–527.

James, E. M., and Browning, N. D. (1999). Practical Aspects of Atomic Resolution Imaging and Analysis in STEM, *Ultramicroscopy* 78:125–139.

Jefferson, D. A. (2000). The Surface Activity of Ultrafine Particles, *Phil. Trans. R. Soc. Lond. A* 358:2683–2692.

Jesson, D. E., and Pennycook, S. J. (1993). Incoherent Imaging of Thin Specimens Using Coherently Scattered Electrons, *Proc. R. Soc. London Ser. A-Math. Phys. Eng. Sci.* 441(1912):261–281.

Kammler, H. K., Madler, L., and Pratsinis, S. E. (2001). Flame Synthesis of Nanoparticles, *Chem. Eng. Technol.* 24(6):583–596.

Keyser, T. R., Natusch, D. F. S., Evans, C. A., Jr., and Linton, R. W. (1978). Characterising the Surface of Environmental Particles, *Environ. Sci. Tech.* 12(7):768–773.

Kim, S. H., Liu, B. Y. H., and Zachariah, M. R. (2002). Synthesis of Nanoporous Metal Oxide Particles by a New Inorganic Matrix Spray Pyrolysis Method, *Chem. Mater.* 14(7):2889–2899.

Lison, D., Lardot, C., Huaux, F., Zanetti, G., and Fubini, B. (1997). Influence of Particle Surface Area on the Toxicity of Insoluble Manganese Dioxide Dusts, *Arch. Toxicol.* 71(12):725–729.

Maximov, I., Gustafsson, A., Hansson, H. C., Samuelson, L., Seifert, W., and Wiedensohler, A. (1993). Fabrication of Quantum-Dot Structures Using Aerosol Deposition and Plasma-Etching Techniques, *J. Vacuum Sci. Technol. A-Vacuum Surfaces Films* 11(4 Pt1):748–753.

Maynard, A. D. (1995a). The Application of Electron Energy-Loss Spectroscopy to the Analysis of Ultrafine Aerosol Particles, *J. Aerosol Sci.* 26(5):757–777.

Maynard, A. D. (1995b). The Development of a New Thermophoretic Precipitator For Scanning-Transmission Electron-Microscope Analysis of Ultrafine Aerosol-Particles, *Aerosol Sci. Technol.* 23(4): 521–533.

Maynard, A. D. (2000). Overview of Methods for Analysing Single Ultrafine Particles, *Phil. Trans. Royal Soc. London Series A-Math. Phys. Eng. Sci.* 358(1775):2593–2609.

Nanda, K. K., Kruis, F. E., Fissan, H., and Acet, M. (2002). Band-Gap Tuning of PbS Nanoparticles by In-Flight Sintering of Size Classified Aerosols, *J. Appl. Phys.* 91(4):2315–2321.

Nellist, P. D., and Pennycook, S. J. (1999). Incoherent Imaging Using Dynamically Scattered Coherent Electrons, *Ultramicroscopy* 78(1–4):111–124.

NIOSH (1988). *NIOSH Criteria for a Recommended Standard: Welding, Brazing, and Thermal Cutting*, DHHS, CDC, NIOSH.

O'Keefe, M. A., Hetherington, C. J. D., Wang, Y. C., Nelson, E. C., Turner, J. H., Kisielowski, C., Malm, J. O., Mueller, R., Ringnalda, J., Pan, M., and Thust, A. (2001). Sub-Angstrom High-Resolution Transmission Electron Microscopy at 300 keV, *Ultramicroscopy* 89(4):215–241.

Oberdörster, G. (2000). Toxicology of Ultrafine Particles: In Vivo Studies, *Phil. Trans. Roy. Soc. London Series A* 358(1775):2719–2740.

Oberdörster, G., Ferin, J., Finkelstein, G., Wade, P., and Corson, N. (1990). Increased Pulmonary Toxicity of Ultrafine Particles. 2. Lung Lavage Studies, *J. Aerosol Sci.* 21(3):384–387.

Oberdörster, G., Gelein, R. M., Ferin, J., and Weiss, B. (1995). Association of Particulate Air Pollution and Acute Mortality: Involvement of Ultrafine Particles? *Inhal. Toxicol.* 7:111–124.

Ostraat, M. L., De Blauwe, J. W., Green, M. L., Bell, L. D., Brongersma, M. L., Casperson, J., Flagan, R. C., and Atwater, H. A. (2001). Synthesis and Characterization of Aerosol Silicon Nanocrystal Nonvolatile Floating-Gate Memory Devices, 79(3):433–435.

Pennycook, S. J., and Boatner, L. A. (1988). Chemically Sensitive Structure-Imaging with a Scanning-Transmission Electron-Microscope, *Nature* 336(6199):565–567.

Peukert, W., Mehler, C., and Gotzinger, M. (2002). Novel Concepts for Characterisation of Heterogeneous Particulate Surfaces, 196(1–4):30–40.

Preining, O. (1998). The Physical Nature of Very, Very Small Particles and Its Impact on Their Behavior, *J. Aerosol Sci.* 29:481–495.

Prost, W., Kruis, F. E., Otten, F., Nielsch, K., Rellinghaus, B., Auer, U., Peled, A., Wassermann, E. F., Fissan, H., and Tegude, F. J. (1998). Monodisperse Aerosol Particle Deposition: Prospects for Nanoelectronics, *Microelectron. Eng.* 42:535–538.

Rafferty, B., and Pennycook, S. J. (1999). Towards Atomic Column-by-Column Spectroscopy, *Ultramicroscopy* 78(1–4):141–151.

Roco, M. C., Williams, S., and Alivisatos, P. (2000). *Nanotechnology Research Directions: IWGN Workshop Report*. Dordrecht, Netherlands, Kluwer Academic Publishers.

Schneider, W. D. (2002). Scanning Tunneling Microscopy and Spectroscopy of Nanostructures, 514(1–3):74–83.

Singh, Y., Javier, J. R. N., Ehrman, S. H., Magnusson, M. H., and Deppert, K. (2002). Approaches to Increasing Yield in Evaporation/Condensation Nanoparticle Generation, *J. Aerosol Sci.* 33(9):1309–1325.

Spurny, K. R., Ed. (1999). *Analytical Chemistry of Aerosols*, Lewis Publishers, Boca Raton.

Tandon, R. K., Payling, R., Chenhall, B. E., Crisp, P. T., Ellis, J., and Baker, R. S. (1985). Application of X-Ray Photoelectron-Spectroscopy to the Analysis of Stainless-Steel Welding Aerosols, *Appl. Surf. Sci.* 20(4):527–537.

Tran, C. L., Buchanan, D., Cullen, R. T., Searl, A., Jones, A. D., and Donaldson, K. (2000). Inhalation of Poorly Soluble Particles. II. Influence of Particle Surface Area on Inflammation and Clearance, *Inhalation Toxicol.* 12(12):1113–1126.

Voitkevich, V. G. (1988). Investigation of Hetereogeneity of Welding Fume Particle Composition by the Method of X-ray Photoelectron Spectroscopy, *Welding in the World, Le Soudage Dans Le Monde* 26(5–6):108–111.

Wallace, W. E., Harrison, J., Keane, M. J., Bolsaitis, P., Epplesheimer, D., Poston, J., and Page, S. J. (1990). Clay Occlusion of Respirable Quartz Particles Detected by Low Voltage Scanning Electron Microscopy—X-Ray Analysis, *Ann. Occupational Hygiene* 34:195–204.

Wegner, K., Stark, W. J., and Pratsinis, S. E. (2002). Flame-Nozzle Synthesis of Nanoparticles with Closely Controlled Size, Morphology and Crystallinity, *Mater. Lett.* 55(5):318–321.

Xhoffer, C., Jacob, W., Buseck, P. R., and Vangrieken, R. (1995). Problems in Quantitatively Analyzing Individual Salt Aerosol-Particles Using Electron-Energy-Loss Spectroscopy, *Spectroc. Acta Pt. B-Atom. Spectr.* 50(10):1281–1292.

Zimmer, A. T., and Biswas, P. (2001). Characterization of the Aerosols Resulting from Arc Welding Processes, *J. Aerosol Sci.* 32(8):1993–1008.